Schweizerischer Erdbebendienst
Service Sismologique Suisse
Servizio Sismico Svizzero
Swiss Seismological Service

ETH zürich

Report on site characterization

Mont Terri, Switzerland (MTI03)

Clotaire Michel, Valerio Poggi, Donat Fäh

Last modified - 10 / 12 / 2014

1. Introduction

In the framework of the MONT TERRI project, SED has installed three seismological stations. Two stations have been installed within the underground rock laboratory located in the security gallery of the Mont Terri motorway tunnel (Canton Jura), roughly 300m b.s.l. The installation consists in a broadband seismometer (MTI02) and a strong-motion sensor (MTI01), both equipped with a high-resolution digitizer (Taurus 24Bit @200sps and 250sps, respectively). The two instruments have been deployed on the opposite sides of the major fault lineament crossing the laboratory (**Figure 1**), in order to monitor seismicity in the region and the activity of the system under fault reactivation by fluid injection in project FS (In situ Clay **F**ault **S**lip hydro-mechanical characterization). The surface installation (MTI03) consists in a strong-motion sensor (Kinemetrics Episensor) equipped with a high-resolution digitizer (Taurus 24Bit @250sps). This instrument has been deployed in a vault at the surface above the underground tunnel, in order to monitor seismicity in the region and the effect of the local geology on ground motion.

To characterize the seismic behavior of the area surrounding the tunnel installation, we review the available documentation with the most significant geophysical experiments performed at the site in the past. For that, an interpretive geophysical model is then provided, which is used for the calculation of the local seismic response at the stations. This document present a summary of the information used to build such model. Moreover, in order to characterize the site of the surface installation, i.e. to estimate a velocity profile below the station, we performed a geophysical measurement (ambient vibration array) on October 2nd, 2014. This document presents the measurement setup, processing and interpretation.

2. Source documentation and data

The literature reviewed in the assessment consisted mostly in the technical reports with the different experiments, the summary activity reports and a list of publications. From the former group of publications, the following documents are of particular interest for the seismic characterization of the site:

- TR2008_04
- TR2000_05
- TR2002_03
- TN2002-44
- TN2000_61
- TN99_62
- TN97_34s
- TN97_33s

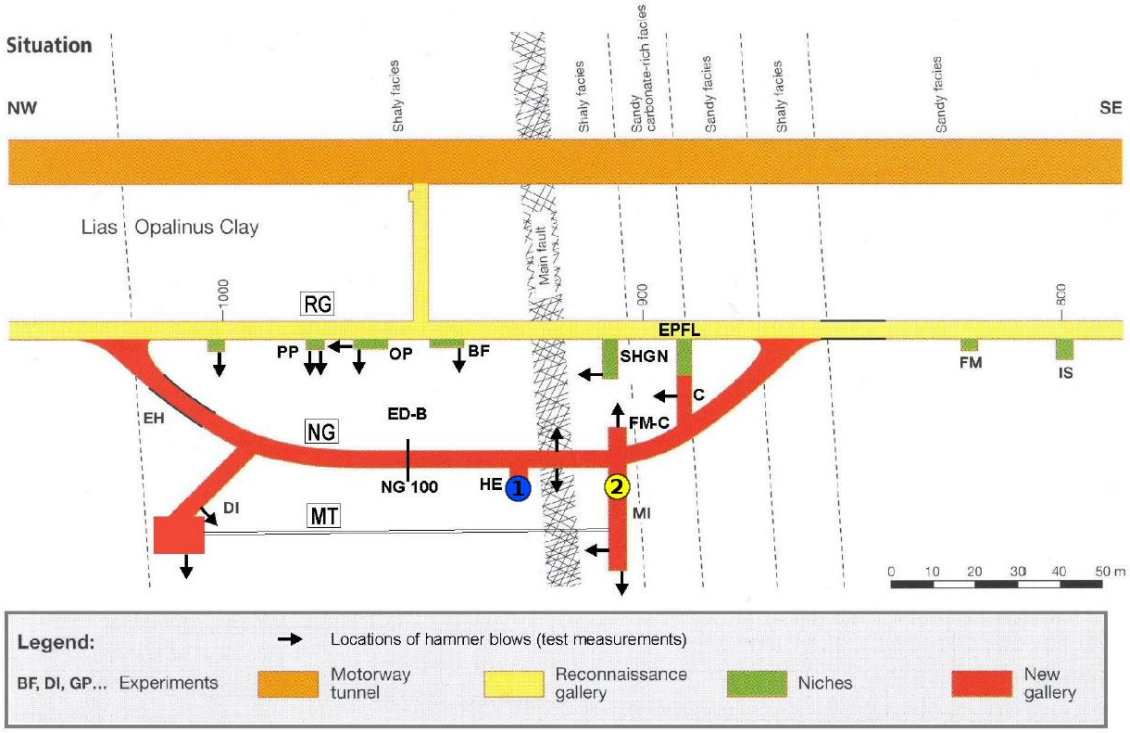

Figure 1 - *Schematic plan of the Mont Terri rock laboratory. The SED seismological stations are indicated with circles, as 1) broad band installation (in blue) and 2) strong motion sensor (in yellow). Between the two sensors the major fault lineament is visible (shaded zone).*

The following summary activity reports include useful information:

- GBD23 - Swiss Geological Survey reports no. 1
- BLGD03 - Swiss Geological Survey reports no. 3
- BWGB4 - Federal Office for Water and Geology reports no. 4

We refer to these reports for a more detailed description of the experiments and the data (including pictures) used in this report.

3. Geology and tectonic setting

From the tectonic perspective, the Mont Terri rock laboratory near St. Ursanne is located within the exposed Mont Terri anticline structure of the folded Jura (**Figure 2** and **Figure 3**). The anticline is made of a sequence of distinct geological units, mostly of Jurassic age, spanning from marl and limestone to clay. Of particular interest for the laboratory is the Opalinus clay formation dating from the earliest Dogger (Aalenian), because of its suitable geomechanical properties in prospect of the installation of a permanent disposal site for radioactive waste in similar material. Both SED stations sit on such formation.

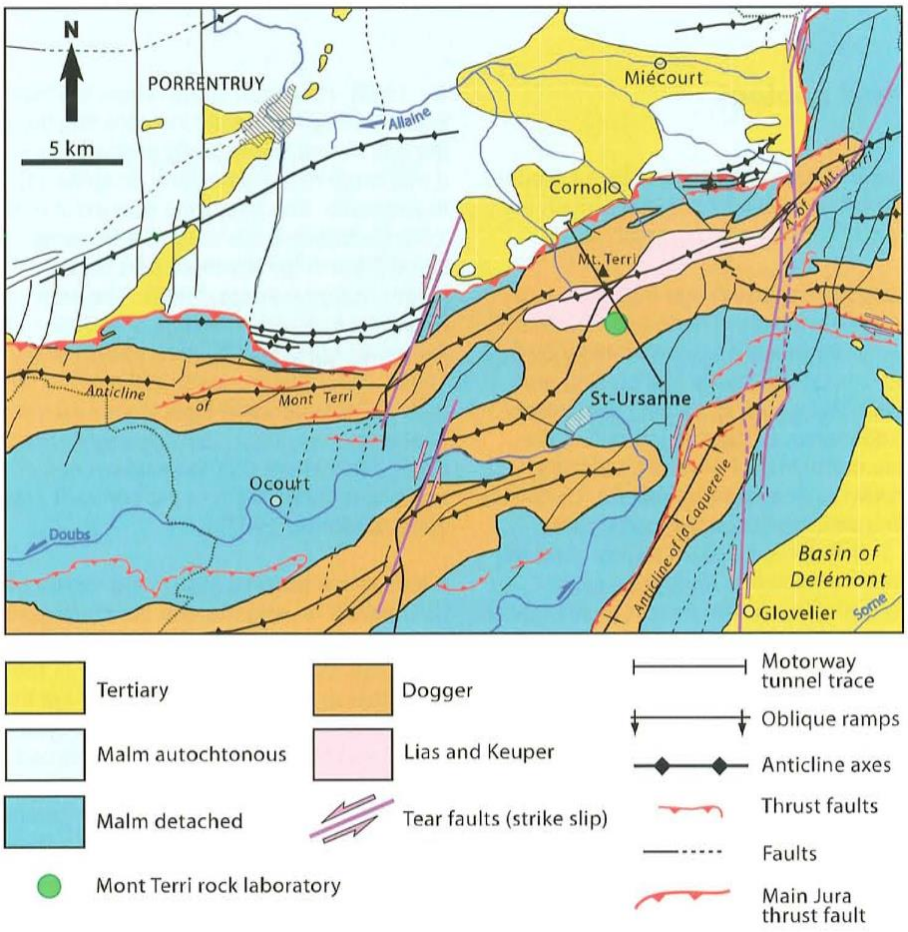

Figure 2 – *Geological/tectonic setting of the folded Jura region in the surrounding of the Mont Terri rock laboratory (modified after Laubscher, 1963).*

The Opalinus clay is a material, which behaves anisotropically due to the thin bedding structure (**Figure 4**). More specifically, the material can be locally approximated with a transverse isotropic model (**Figure 5**); however, its mechanical properties are further complicated by the presence of dense fracturing and faulting induced by local tectonic stresses (**Figure 4**) and excavation. This determines a complex seismic behavior of the material, which cannot be characterized using standard seismic techniques (e.g. refraction of VSP analysis).

4. Input data of the model

Average properties of the Opalinus clay from geophysical laboratory tests can be described as a set of unique values plus uncertainty, as in **Table 1**. These values can be considered representative for the Mont Terri region (ambient conditions with an overburden of about 250 m). However, due to the excavation of the tunnel - which produced a disturbed zone of about 1m width - these homogeneous values cannot be directly used to build the local reference model. Due to the unloading of the lithostatic confining pressure, the velocity values drop significantly close to the gallery wall, as confirmed by several seismic borehole experiments perpendicular to the tunnel axis. Such variability has to be taken into account by providing simplified one-dimensional velocity profiles along the minimum and maximum velocity direction of the Opalinus clay formation.

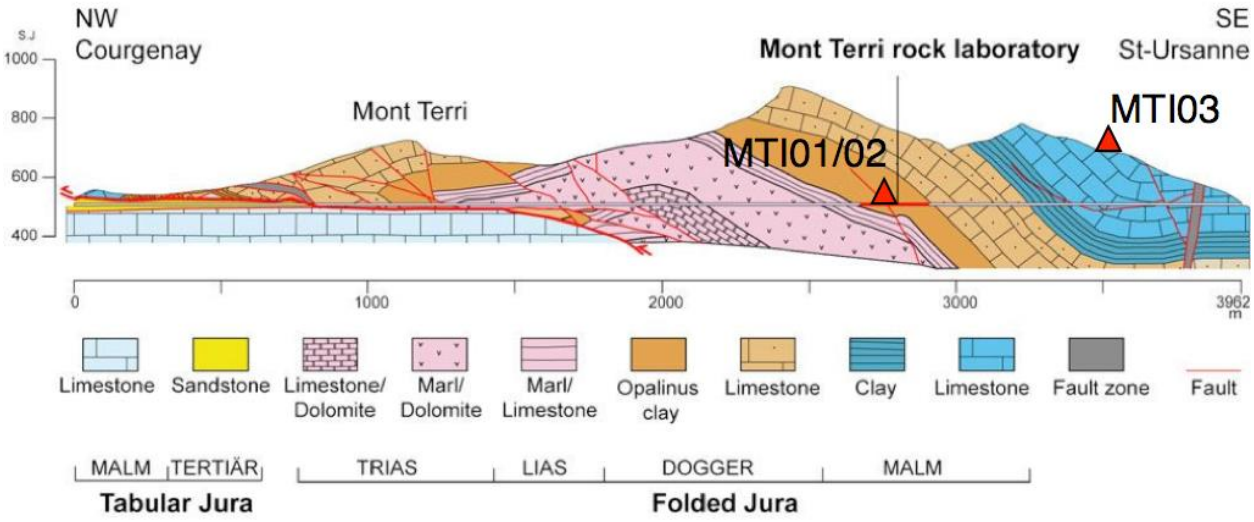

Figure 3 – *Interpretative cross-section of the Mont Terri anticline at the rock laboratory (after Freivogel & Huggenberger, 2003). The major fault lineament crossing the laboratory is visible in thin red, SED stations were added as red triangles.*

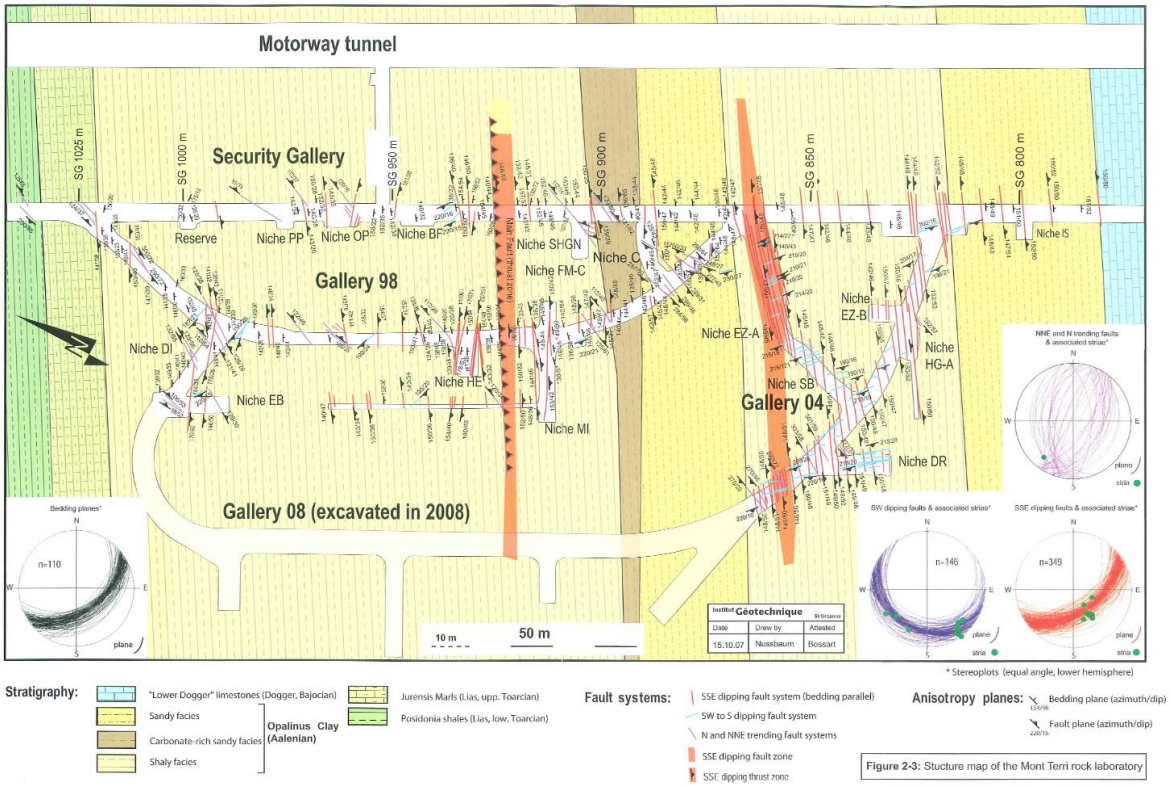

Figure 4 – *Orientation of bedding and fault planes within the Opalinus clay along the laboratory tunnels.*

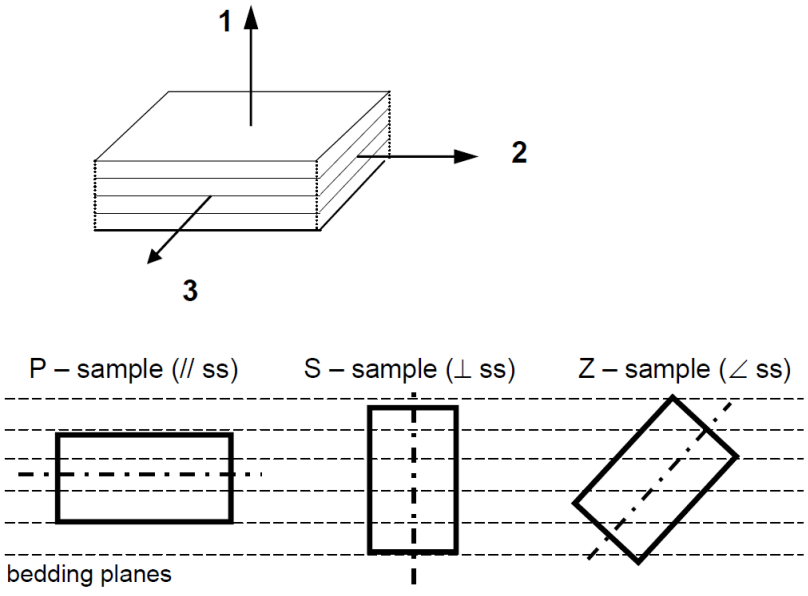

Figure 5 – *Schematic showing the direction conventions used to describe transverse isotropy.*

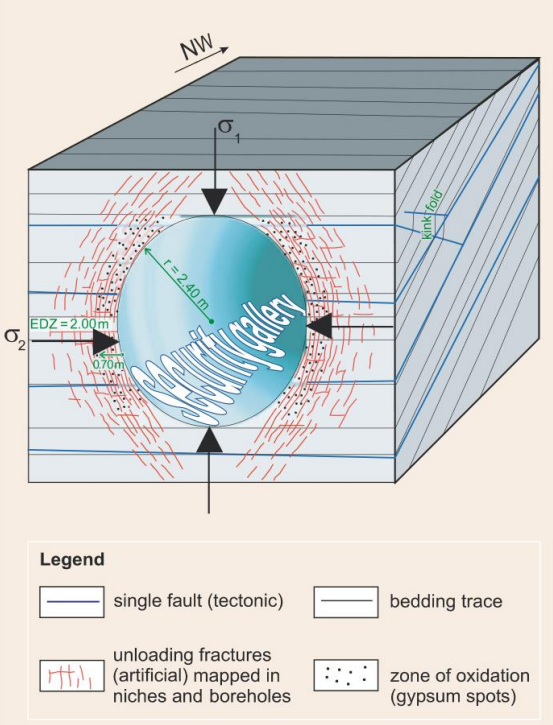

Figure 6 – *Example sketch showing the different type of mechanical discontinuity around the excavation disturbed zone (after Bossart & Adler, 1999).*

Minimum P- and S-wave velocity values for the Excavation Disturbed Zone (EDZ) have been established by comparison of different available seismic borehole logs (from reports). However, such results are meant to be qualitative estimations, and therefore possibly biased by a large uncertainty (**Table 2**), yet not defined. For the density we assumed a value at the EDZ corresponding to dry Bulk density, as obtained directly from laboratory tests (about 100 Kg/m^3 less than standard conditions).

The decay curves for the velocity and the density values were conditioned by the average behavior observed from the seismic logs (see appendix for examples). As assumption, we impose the standard undisturbed values (**Table 1**) to progressively drop to the corresponding EDZ value (**Table 2**) by means of a smooth gradient decay starting from about 1m from the tunnel wall and with corner (the change in decay slope) at 0.5m. **Figure 7** provides a schematic representation of the decay model.

Recommended values		
Parameter	**Mean**	**Error**
Vp // ss	3350 (m/s)	± 150 (m/s)
Vp ⊥ ss	2620 (m/s)	± 150 (m/s)
Vs // ss	1920 (m/s)	± 100 (m/s)
Vs ⊥ ss	1510 (m/s)	± 50 (m/s)
ρ	2430 (kg/m^3)	± 20 (kg/m^3)

Table 1 – *Average elastic parameters for Opalinus clay formation. Direction conventions are as in* ***Figure 5*** *(from technical report 2008-4)*.

Estimated minimum values (EDZ)		
Parameter	**Mean**	**Error**
Vp // ss	2600 (m/s)	--
Vp ⊥ ss	1500 (m/s)	--
Vs // ss	1400 (m/s)	--
Vs ⊥ ss	1000 (m/s)	--
ρ	2330 (kg/m^3)	± 50 (kg/m^3)

Table 2 – *Estimated elastic parameters for Opalinus clay formation in the excavation disturbed zone. Direction conventions are as in* ***Figure 5*** *(from technical report 2008-4)*.

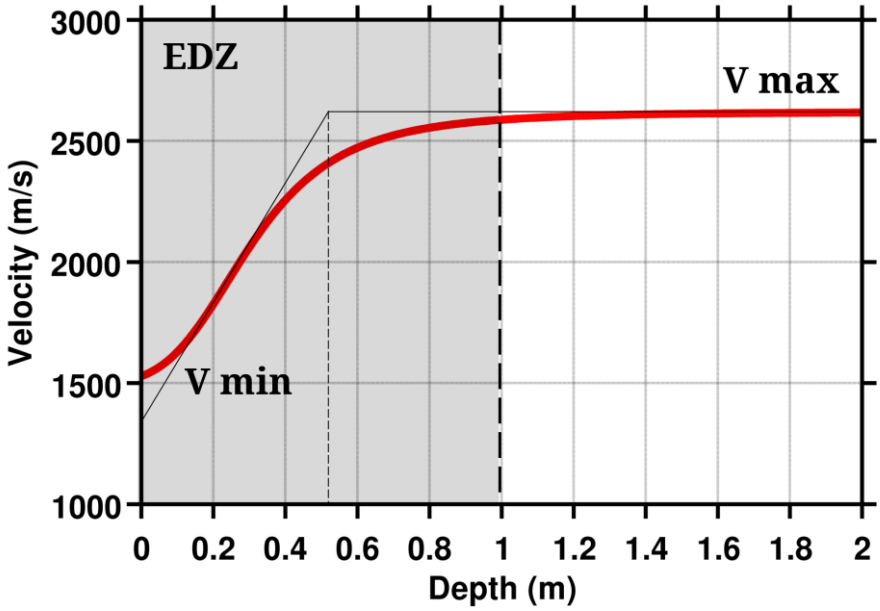

Figure 7 – *Schematic representation of the velocity decay function at the EDZ. Vmax and Vmin are constrained by estimated values in* **Table 1** *and* **Table 2**.

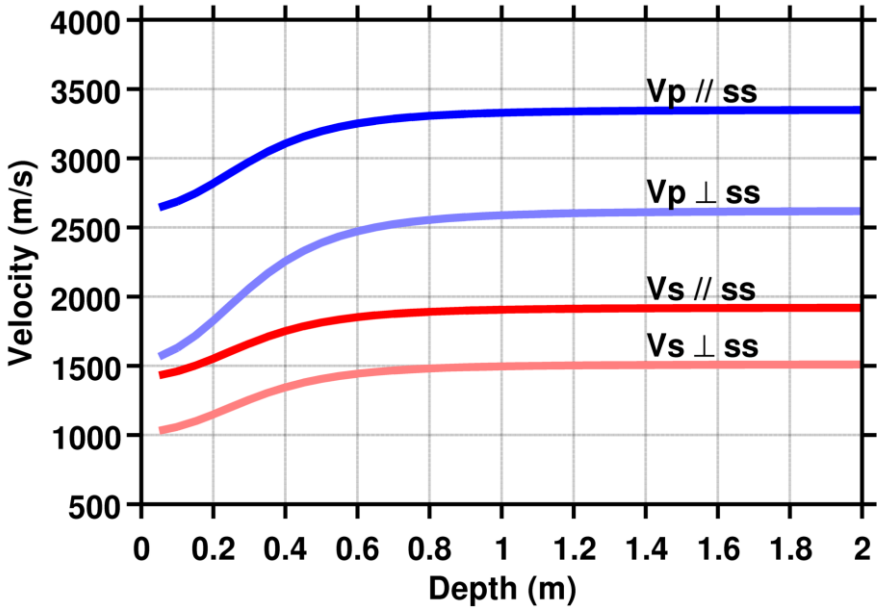

Figure 8 – *Comparison between velocity decay functions at the EDZ for the P and S components and for different directions of the material.*

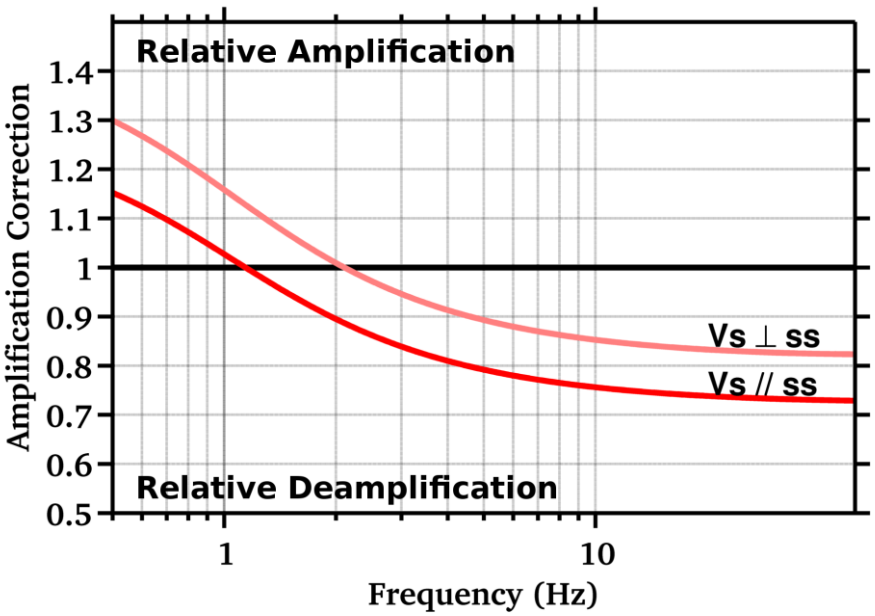

Figure 9 – *Correction functions for the two main directions of the Oplinus clay with respect to the Swiss reference rock conditions (Poggi et al., 2011). The simplified model assumes the tunnel wall as free surface and radial one-dimensional propagation.*

5. Seismic response calculation

In a first attempt, seismic response of the tunnel has been estimated using SH-wave transfer function formalism, assuming orthogonal incidence to the tunnel (modeled as free surface) and one-dimensional propagation. The corresponding amplification function is nevertheless flat and equal to one for the whole range of frequencies of engineering interests (0.5-50Hz), since the effect of EDZ has impact only at very high frequencies. The final response, corrected for the Swiss reference conditions (Poggi et al., 2011), is given in **Figure 9** (separately for the two anisotropy directions of the Opalinus Clay formation).

Such model, however, represents an oversimplification of the true response, since it does not take into account the contribution of reflected phases at the surface. A better numerical model will be subsequently defined, after incorporation of the incoming information about sub-surface geology.

6. Experiment description

Ambient vibrations

The ground surface is permanently subjected to ambient vibrations due to:

- natural sources (ocean and large-scale atmospheric phenomena) below 1 Hz,
- local meteorological conditions (wind and rain) at frequencies around 1 Hz ,
- human activities (industrial machines, traffic. . .) at frequencies above 1 Hz [Bonnefoy-Claudet et al., 2006].

The objective of the measurements is to record these ambient vibrations and to use their propagation properties to infer the underground structure. First, the polarization of the recorded waves (H/V ratio) is used to derive the resonance frequencies of the soil column. Second, the arrival time delays at many different stations are used to derive the velocity of surface waves at different frequencies (dispersion). The information (H/V, dispersion curves) is then used to derive the properties of the soil column using an inversion process.

Equipment

For these measurements 12 Quanterra Q330 dataloggers named NR01 to NR12 and 14 Lennartz 3C 5 s seismometers were used. Each datalogger can record on 2 ports A (channels EH1, EH2, EH3 for Z, N, E directions) and B (channels EH4, EH5, EH6 for Z, N, E directions). Time synchronization was ensured by GPS. The sensors were placed on a metal tripod, in a 20 cm deep hole, when necessary, for better coupling with the ground.

Geometry of the arrays

Two array configurations were used, for a total of 4 rings of 10, 25, 50 and 100 m radius around a central station. The first configuration includes the 3 inner rings with 14 sensors; the second configuration includes the 2 outer rings with 11 sensors. The minimum inter-station distance and the aperture are therefore 10 and 100 m and 50 and 200 m, respectively. The experimental setup is displayed in **Figure 10**. The final usable datasets are detailed in the next section.

Positioning of the stations

The sensor coordinates were measured using a differential GPS device (Leica Viva GS10), including only a rover station and using the Real Time Kinematic technique provided by *Swisstopo*. It allows an absolute positioning with accuracy better than 4 cm on the Cartesian Swissgrid.

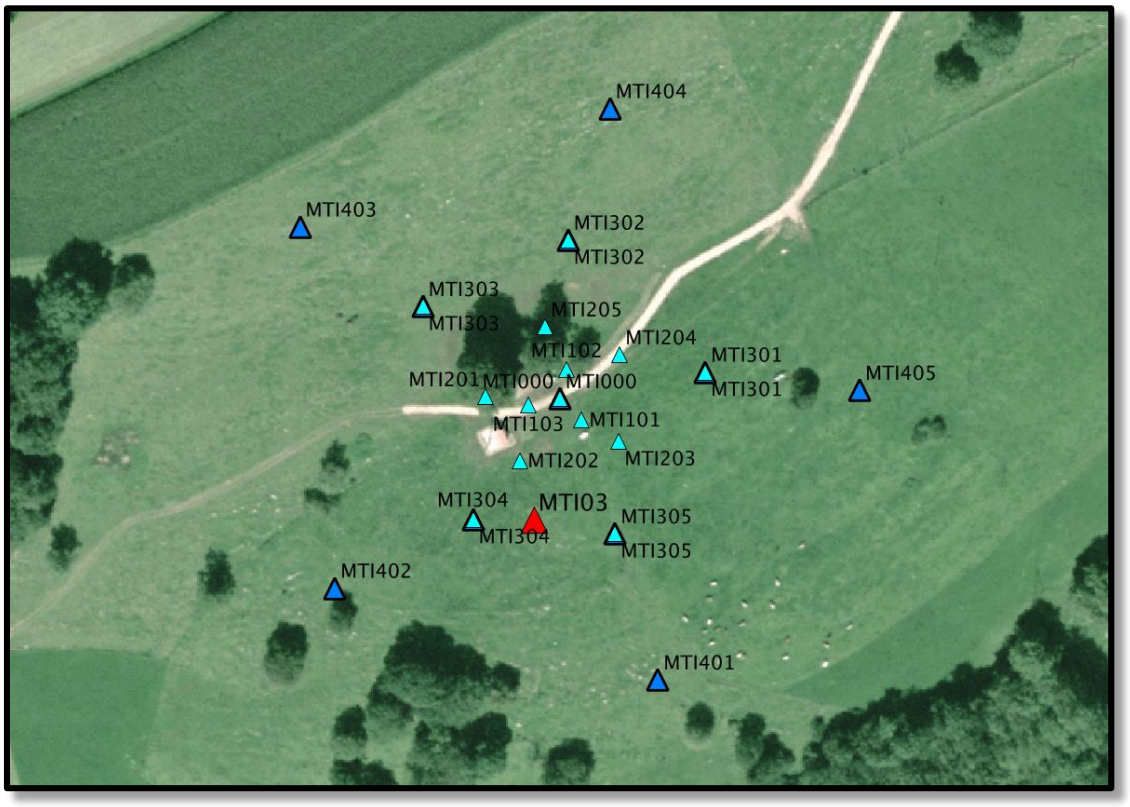

Figure 10 - *Geometry of the arrays. Light blue triangles refer to the first configuration while triangles with thick border refer to the second configuration. Permanent station MTI03 is the red triangle.*

Figure 11 – *View of the experiment; the central station was located along the path.*

7. Data quality

Usable data

The largest time windows were extracted, for which all the sensors of the array were correctly placed and the GPS synchronization was ensured. The recording at station MTI304 on the N component did not work (possibly due to a cable problem) for both datasets.

During dataset 1, wind was blowing constantly. Wind got weaker during dataset 2 though still present. A tractor disturbed the recordings, starting at 13:00 in the field located north of the array, and progressively approaching during the acquisition. During the same dataset, cows approached the array. Sensor MTI401 has been toppled by a cow at 13:30, set back at 13:37, but toppled again shortly after. Therefore, 2 sets have been extracted for dataset 2, a short one until 13:29 and a longer one until 13:47 where MTI401 cannot be used. On the recording at station MTI102 on all 3 components, very large undamped peaks are seen at 0.8, 1.56, 2.34, 3.13, 3.91, 4.68, 5.48, 6.24, 7.05, 7.82, 8.58 and 9.38 Hz. The effect is very local since no other sensor is affected. An explanation could be a buried electric cable powering the field fence. This station was therefore not be used in the processing. Apart from these issues, the recordings are overall of good quality.

Orientations of the sensors were checked by maximizing the correlation with the central station at low frequencies [Poggi et al., 2012]. Deviations lower than 10° were found for all points but MTI203 (15°). Original and rotated datasets are available for the 3C array analysis. The characteristics of the datasets are detailed in **Table 3**.

Dataset	Starting date	Time	Length	Fs	# of points
1	2014/10/02	09:45	119 min	200 Hz	14
2 short	2014/10/02	12:13	76 min	200 Hz	11
2 long	2014/10/02	12:13	94 min	200 Hz	10

Table 3 – *Available datasets for processing*

Data pre-processing

The data were first converted to SAC format including in the header the coordinates of the point (CH1903 system), the recording component and a name related to the position. The name is made of 3 letters characterizing the location (MTI here), 1 digit for the ring and 2 more digits for the number in the ring. Recordings were not corrected for the instrumental response.

8. H/V processing

Processing methods and parameters

In order to process the H/V spectral ratios, several codes and methods were used. The classical H/V method was applied using the Geopsy (http://www.geopsy.org) software. In this method, the ratio of the smoothed Fourier Transform of selected time windows are averaged. Tukey windows (cosine taper of 5% width) of 50 s long overlapping by 50% were selected. Konno and Ohmachi [1998] smoothing procedure was used with a b value of 60. The classical method computed using the method of Fäh et al. [2001] was also performed.

Moreover, the time-frequency analysis method [Fäh et al., 2009] was used to estimate the ellipticity function more accurately using the Matlab code of V. Poggi. In this method, the time-frequency analysis using the Wavelet transform is computed for each component. For each frequency, the maxima over time (10 per minute with at least 0.1 s between each) in the TFA are determined. The Horizontal to Vertical ratio of amplitudes for each maximum is then computed and statistical properties for each frequency are derived. A Cosine wavelet with parameter 9 is used. The mean of the distribution for each frequency is stored. For the sake of comparison, the time-frequency analysis of Fäh et al. [2001], based on the spectrogram, was also used.

The ellipticity extraction using the Capon analysis [Poggi and Fäh, 2010] (see section on array analysis) was also performed.

Results

All points show the same H/V ratios. All differences may be related to inappropriate sensor placements (**Figure 12**). In particular, the amplitudes on the N and E components of point MTI000 are different probably due to a lack of horizontality. The fundamental peak is broad with a peak value at 0.9 Hz with amplitudes of about 4. A small peak can be seen at 2.5 Hz.

Moreover, all the methods to compute H/V ratios are compared close to the array centre in **Figure 13**, in which the classical methods were divided by $\sqrt{2}$ to correct from the Love waves contribution [Fäh et al., 2001]. This comparison shows that the TFA methods in this case did not remove the Love wave contribution since their

corresponding curves have larger values than the 3C FK analysis (Capon method), which matches well the classical methods divided by $\sqrt{2}$, although it does not have resolution down to the peak. Above 5 Hz, the Love wave contribution may be smaller since the FK analysis lies above the classical methods divided by $\sqrt{2}$.The 3C FK analysis highlights the peak at 2.5 Hz that is hardly seen on the classical methods, as well as its subsequent trough. This is however clear to see on dataset 2 but less clear on dataset 1.

The fundamental peak at the MTI03 station is therefore at 0.9 Hz, with a peak amplitude around 3.

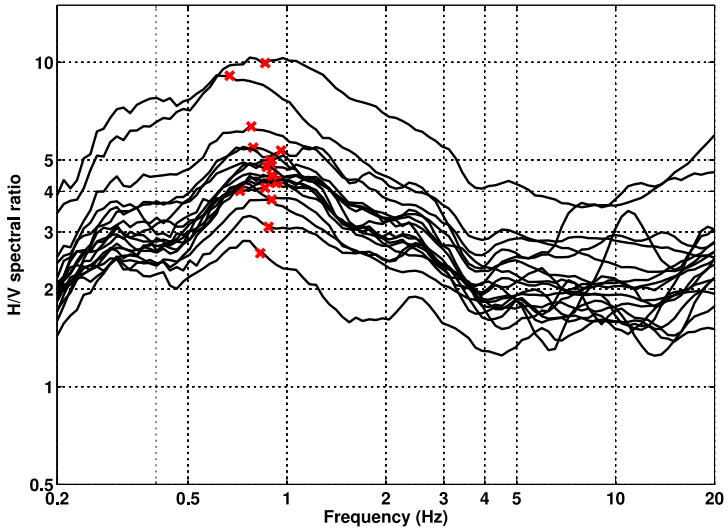

Figure 12 – *H/V spectral ratios (TFA code V. Poggi) for all points of the experiment but MTI102 and picking of the fundamental frequency.*

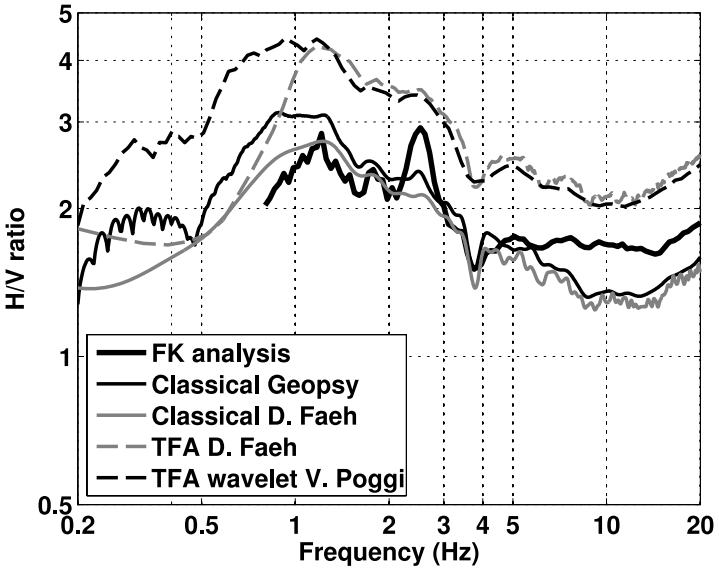

Figure 13 – *H/V spectral ratios for point MTI101 for different codes. Classical methods were divided by* $\sqrt{2}$.

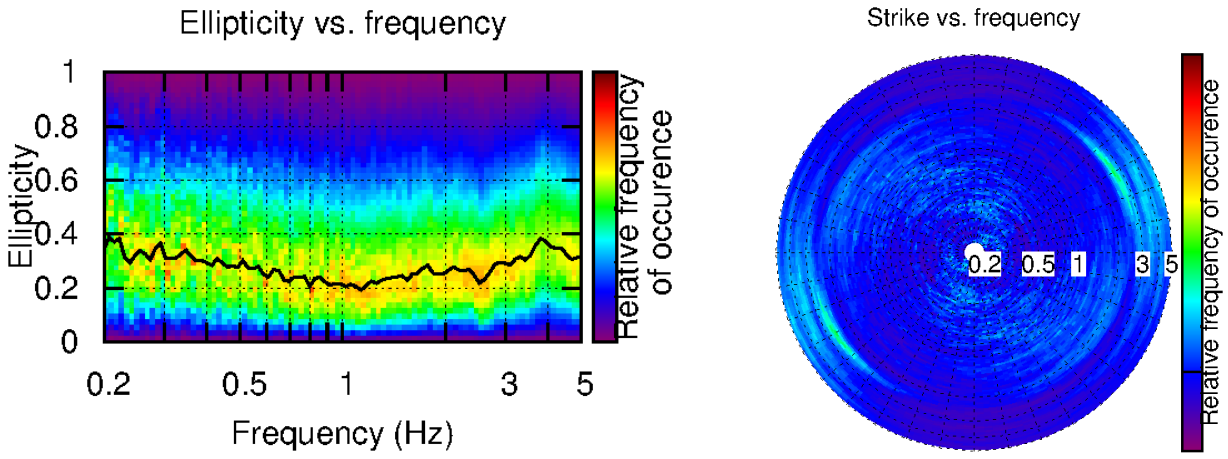

Figure 14 – *Polarization analysis at point MTI303. Left: Ellipticity (A trough in the ellipticity corresponds to polarized motion). Right: Strike of the polarization.*

9. Array processing

Processing methods and parameters

The data were processed between 0.8 and 25 Hz. The vertical components of the arrays were processed using the High-resolution FK analysis [Capon, 1969] using the Geopsy (http://www.geopsy.org) software. Large time windows (300T) were used along with a grid of wave-numbers up to 0.6 with a 0.001 resolution.

Moreover, a 3C array analysis [Fäh et al., 2008] was also performed using the array_tol_3C software [Poggi and Fäh, 2010] between 600 and 4000 m/s. It allows deriving Rayleigh and Love dispersion curves including the Rayleigh ellipticity.

Polarization analysis

We looked for polarization of wavefield in order to detect eventual 2D effects (**Figure 14**). Polarization analysis on the array data was performed using the method of Burjánek et al. [2010]. Apart of the bad quality recordings, all points show a polarization in the NE-SW direction. It corresponds to the longitudinal direction of the mountain ridge where the station is located, but it also corresponds to the direction of the highway tunnel. This polarization is therefore most probably due to the traffic in the tunnel.

Obtained dispersion curves

The picking and interpretation of the curves was performed iteratively with the inversion, using data of all datasets and several processing parameters, not all detailed here. Tests with and without point MTI102, that shows anthropogenic disturbances, did not show noticeable differences. Moreover, computations for dataset 2 showed that the longer recording with one sensor less was providing slightly better results.

Finally, the fundamental Rayleigh mode was picked on dataset 2 between 3.3 Hz and 9 Hz (**Figure 15**). The velocities are ranging from 1900 m/s at 3.3 Hz down to 1000 m/s at 9 Hz. A first higher mode is visible on dataset 1 only and was picked between 6 and 9 Hz. Energy in between these two modes can be clearly seen on dataset 2, it was interpreted as mix of these two and therefore not picked.

On the transverse component of the 3C analysis, fundamental Love mode is picked in a similar frequency range as Rayleigh but with lower velocities (from 1700 m/s at 3.3 Hz down to 700 m/s at 10 Hz). On the radial component, the same mode as Love is seen, which could be due to the failed decomposition of the horizontal components. It may be due to misorientation of sensors that was difficult to correct in some cases. However, the obtained ellipticity curve of Rayleigh waves (**Figure 16**) is consistent with the other H/V computations (**Figure 13**). All picked curves are presented together on **Figure 17**.

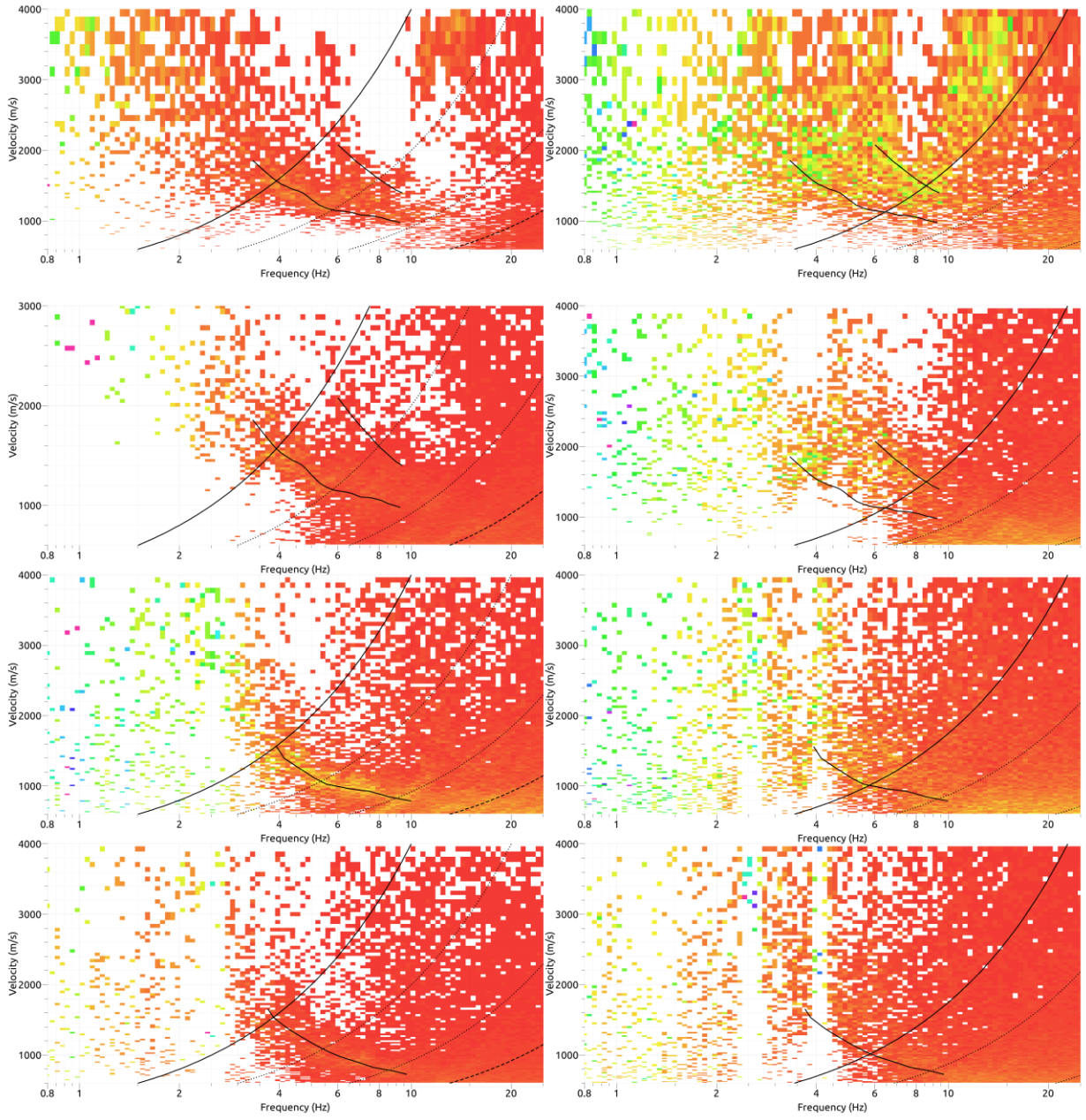

Figure 15 – *Dispersion curves obtained from the 1C and 3C array analyses (from top to bottom: vertical 1C, vertical 3C, radial, transverse components; left: dataset 2; right: dataset 1).*

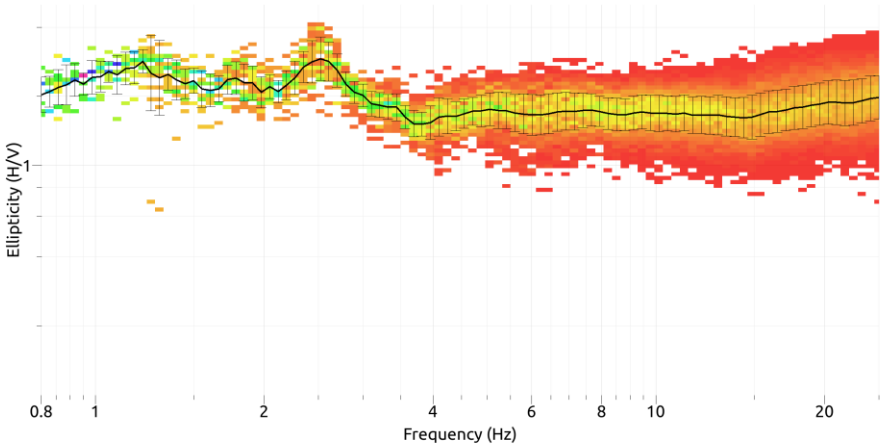

Figure 16 – *Ellipticity curve obtained from the 3C array analysis*

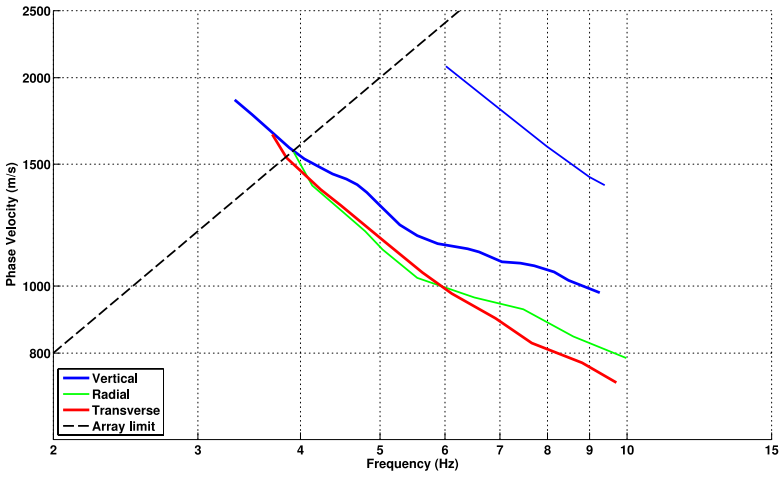

Figure 17 – *Picked dispersion curves.*

10. Inversion and interpretation

Geological context

The performed array around MTI03 station is located on limestone of Kimmeridgian age (Upper Jurassic-Malm) (see **Figure 3** and **Figure 18**). The installation of the station showed that the limestone was weathered at the surface (picture on the left), as noticed on the geological map with the yellow zone. Following the geological map and assuming the layers are flat in the southern part of the hill, the sequence of layers (Malm only) should be approximately:

- 70m of Kimmeridgian limestone
- 40m of Middle and Upper Sequanian limestone and marls
- 30m of Lower Sequanian marl
- Rauracian (Upper Oxfordian) limestone

It should be noticed that Sequanian age is actually overlapping Upper Oxfordian and Lower Kimmerdigian. As a result for the interpretation of our experiment, the anisotropy of the Opalinus clay, located more than 400m below the surface, should not play a role in the ground motion observed at the station MTI03.

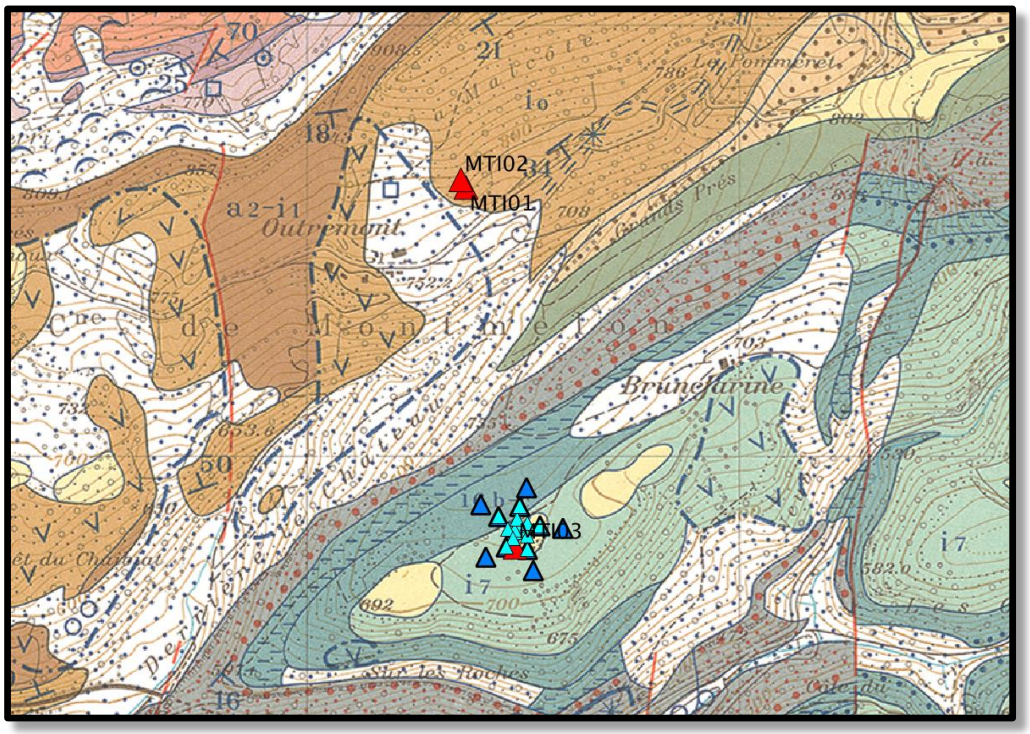

Figure 18 – *Geological map (Swisstopo) with the permanent stations of SED (red triangles) and the stations of the experiment (blue triangles).*

Inversion

For the inversion, Rayleigh and Love fundamental and the first higher Rayleigh mode dispersion curves without standard deviation to avoid different weighting as well as the ellipticity curve from the 3C FK analysis were used. All curves were resampled using 50 points between 1 and 20 Hz in log scale. The inversion was performed using the Improved Neighborhood Algorithm (NA) Wathelet [2008] implemented in the Dinver software. In this algorithm, the tuning parameters are the following: N_{s0} is the number of starting models, randomly distributed in the parameter space, N_r is the number of best cells considered around these N_{s0} models, N_s is the number of new cells generated in the neighborhood of the N_r cells (N_s/N_r per cell) and It_{max} is the number of iteration of this process. The process ends with $N_{s0} + N_r * N_s/N_r * It_{max}$ models. The values for It_{max}, N_{s0}, N_s and N_r are in these computations 500, 10000, 100 and 100, respectively.

During the inversion process, low velocity zones were not allowed. The maximal allowed velocity is set at 3200 m/s (crustal velocity), although this velocity is actually not expected to be reached in limestone. The maximum explored depth is in the order of 200-300 m. The fundamental frequency peak at 0.9 Hz corresponds however possibly to a layer at about 600 m depth. Deeper models were tested in order to reproduce this peak without success. The Poisson ratio was inverted in each layer in the range 0.2-0.4. The density was supposed equal to 2500 kg/m3 for all layers. Inversions with free layer depths as well as fixed layer depths were performed. 4 layers are enough to explain most of the targets (dispersion and ellipticity), but more layers are used to smooth the obtained results and better explore the parameter space. 5 independent runs of 5 different parameterization schemes (4 and 6 layers over a half space and 11 to 12 layers with fixed depth) were performed (**Figure 19** and **Figure 20**). For further elaborations, the best models of these 25 runs were selected (**Figure 21**).

The first 30 m are found to be weathered with velocities of about 800 m/s. The inversion shows velocities lower than 500 m/s in the 5 first meters. Although the first 15 m are not well constrained by the data, low velocities are necessary to pull down the dispersion curves and the flat ellipticity at high frequencies shows that this decrease is gradual. The obtained models are therefore realistic but could be refined with shallow active seismics. Below, the velocity is relatively stable around 1500 m/s (hard rock). No evidence of velocity inversion in the data exists, though it cannot be excluded in this part. At about 140 m depth, the velocity increases again but the data do not constrain this increase anymore. This interface at 140 m depth is producing the small peak at 2.5 Hz in the ellipticity. Moreover, it could correspond to the interface between the Sequanian and the Rauracian. This last layer has a compact limestone bank on its top part that could produce the velocity contrast with respect to the Lower Sequanian marls.

When comparing to the target curves (**Figure 19** and **Figure 20**), all curves are well represented.

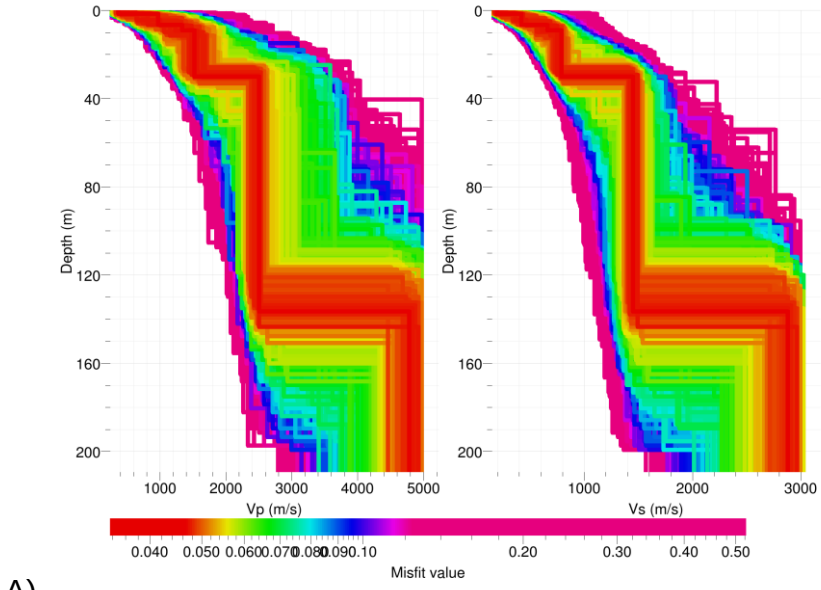

A)

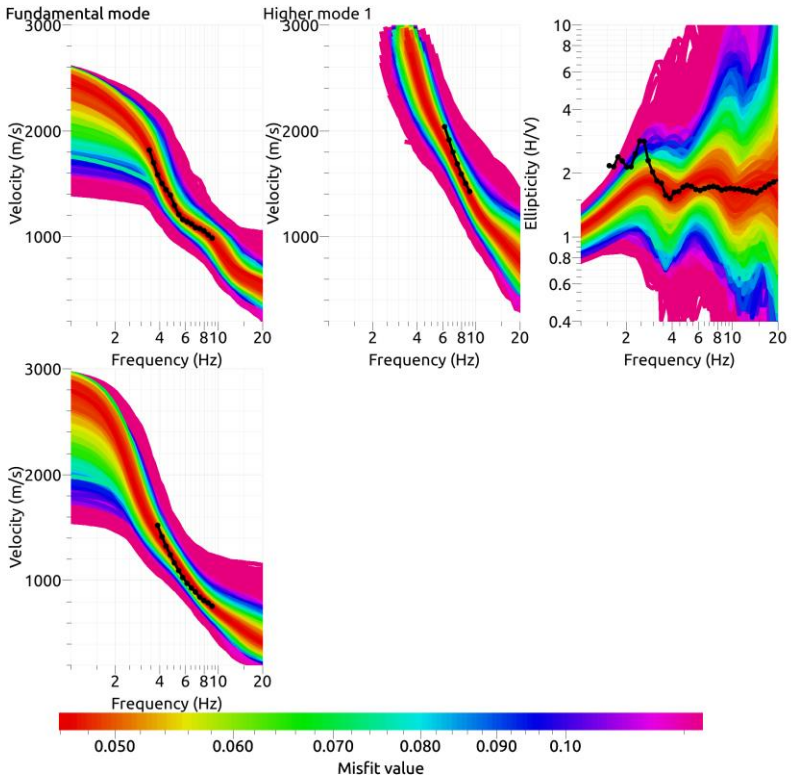

B)

Figure 19 – *Inverted ground profiles in terms of Vp and Vs (top) and comparison between inverted models and measured Rayleigh and Love modes and corresponding ellipticity, free layer depth strategy.*

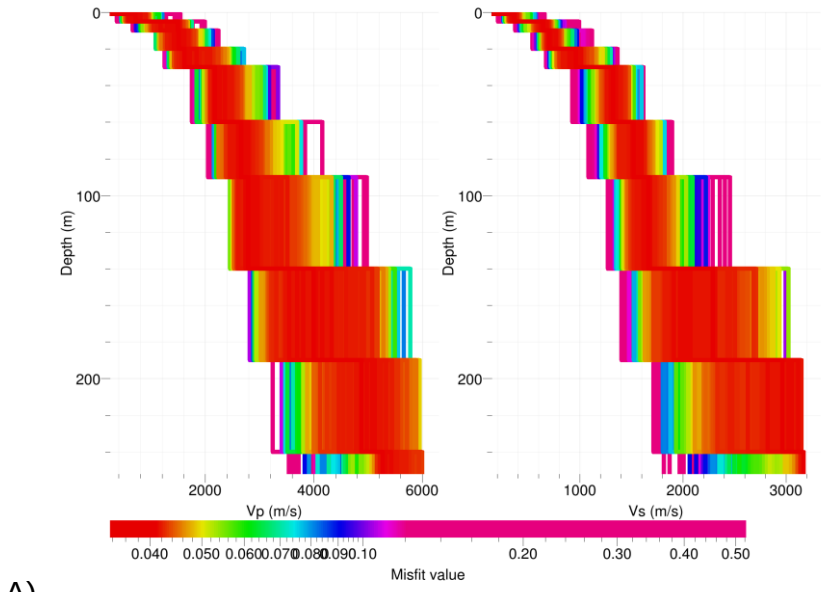

A)

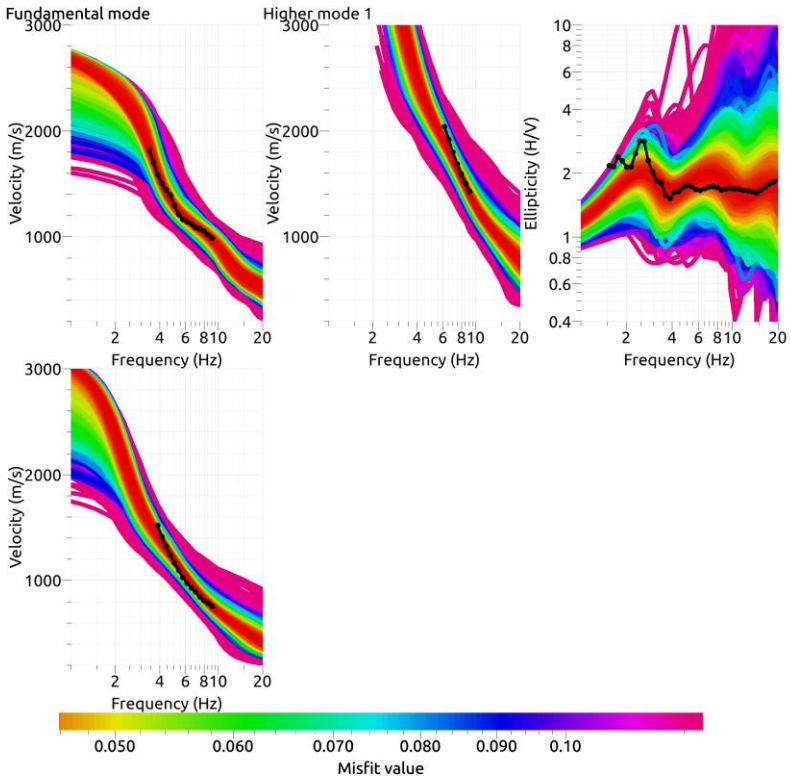

B)

Figure 20 – *Inverted ground profiles in terms of Vp and Vs (top) and comparison between inverted models and measured Rayleigh and Love modes and corresponding ellipticity, fixed layer depthstrategy.*

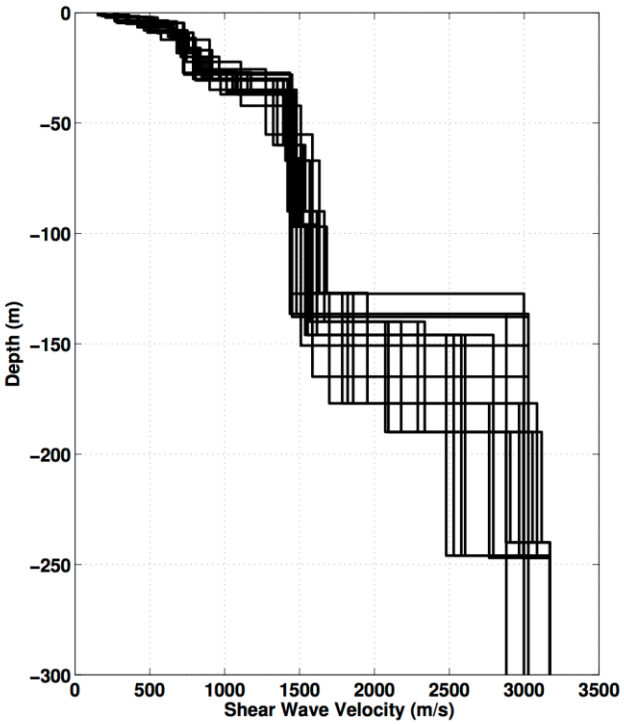

Figure 21 – *V_S ground profiles for the selected 25 best models*

	Mean (m/s)	Uncertainty (m/s)
$V_{s,5}$	299	10
$V_{s,10}$	401	14
$V_{s,20}$	522	10
$V_{s,30}$	604	9
$V_{s,40}$	696	9
$V_{s,50}$	775	8
$V_{s,100}$	1018	7
$V_{s,150}$	1172	10
$V_{s,200}$	1355	25

Table 4 – *Travel time averages at different depths from the inverted models. Uncertainty is given as one standard deviation from the selected profiles.*

Travel time average velocities and ground type

The distribution of the travel time average velocities at different depths was computed from the selected models. The uncertainty, computed as the standard deviation of the distribution of travel time average velocities for the considered models, is also provided, but it does not cover all the uncertainty on these profiles. $V_{S,30}$ is found to be 604 m/s, which corresponds to class B in the Eurocode 8 [CEN, 2004] and SIA261 [SIA, 2003]. However, the site would be classified as type E for SIA261 since about 5 m seems to have a low velocity on layers with velocities higher than 800 m/s.

SH-wave transfer function

The theoretical SH-wave transfer function for vertical propagation [Roesset, 1970] is computed from the inverted profiles and corrected for the Swiss reference [Poggi et al., 2011] (**Figure 22**). In this case, the models are predicting a small amplification with respect to the Swiss reference rock increasing with frequency and showing peaks at 2.5, 6.2 and 15 Hz with factors of 1.6, 2.4 and 2.8, respectively.

It can be compared to the preliminary amplification function obtained by empirical spectral modeling (ESM) [Edwards et al., 2013], obtained with the first earthquake recordings on the permanent station (**Figure 22**). 2 to 3 events only, depending on the frequency, could be used to build the function presented here, which is not enough to obtain a reliable curve, especially its absolute amplitude. Nevertheless, the comparison shows a good match above 5 Hz (position of the peaks and their amplitudes). It can be noticed that the relatively high amplification at high frequencies confirms the low velocities at the surface. At lower frequency, the peak at 2.5 Hz is not seen but the 1 Hz peak from the H/V ratios may be also recognized on the ESM function.

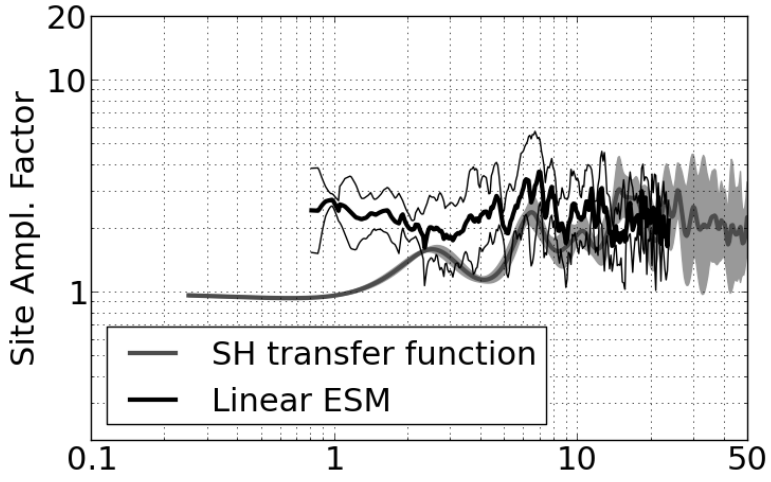

Figure 22 – *Theoretical SH transfer function with its standard deviation (grey line and shade) and preliminary ESM amplification function with its standard deviation (black curves)*

Conclusion on the characterization of the surface station

The array measurements presented in this study were successful in deriving a velocity model for the Mont Terri surface site in Saint-Ursanne, below the MTI03 station. We found a layer of weathered limestone at the surface of about 30 m thickness with velocities of about 800 m/s. The first 5 m show low values but are not well constrained by our data and could be refined using shallow active seismic. Below, the velocity is about 1500 m/s until an interface at about 140 m depth. This interface is producing a small peak at 2.5 Hz in the ellipticity and the amplification function. The fundamental frequency of the H/V peak at 0.9 Hz, probably due to a deeper interface, cannot be reproduced with our data. $V_{S,30}$ is found to be close to 600 m/s. The EC8 and SIA261 ground types are B and E, respectively. The first recordings on the station show a good match with the proposed 1D models, though more recordings are needed to validate them.

11. Computation of the ground motion at depth

To estimate the interference patterns (due to summations of waves reflected at the surface) on the ground motion at 300m depth, the rock velocity model for the laboratory had to be extended to the free surface. Since it was not realistic to assume (homogenous) constant velocity over the whole profile, it was decided to merge the rock velocity model with that from ambient vibration analysis, this last considered well representative of near-surface conditions (including the effect of lithostatic unloading and weathering).

However, merging of the models presented some difficulties. As first, the two models are representative of different locations, distant about 800m, and therefore not well aligned along the vertical. Joining the profiles required then some interpretation on where to cut the different models. Moreover, the transversal isotropy of the rock material led to the coexistence of two complementary profiles, nevertheless considered as upper and lower velocity bounds of the interpreted extended profiles. Moreover, the laboratory cavity represents a discontinuity along the profile, where special boundary conditions should be properly defined. For simplicity, however, the effect of the discontinuity was neglected by virtually collapsing the diameter of the tunnel to zero. This is a reasonable assumption for wavelength much larger than the tunnel section.

The resulting velocity models are gradient-like, with larger variations of velocity in the first 100m, followed by the constant velocity of the rock (different for the two orthogonal directions). At the tunnel depth, velocity is assumed to drop, according to experimental evidences (**Figure 23**).

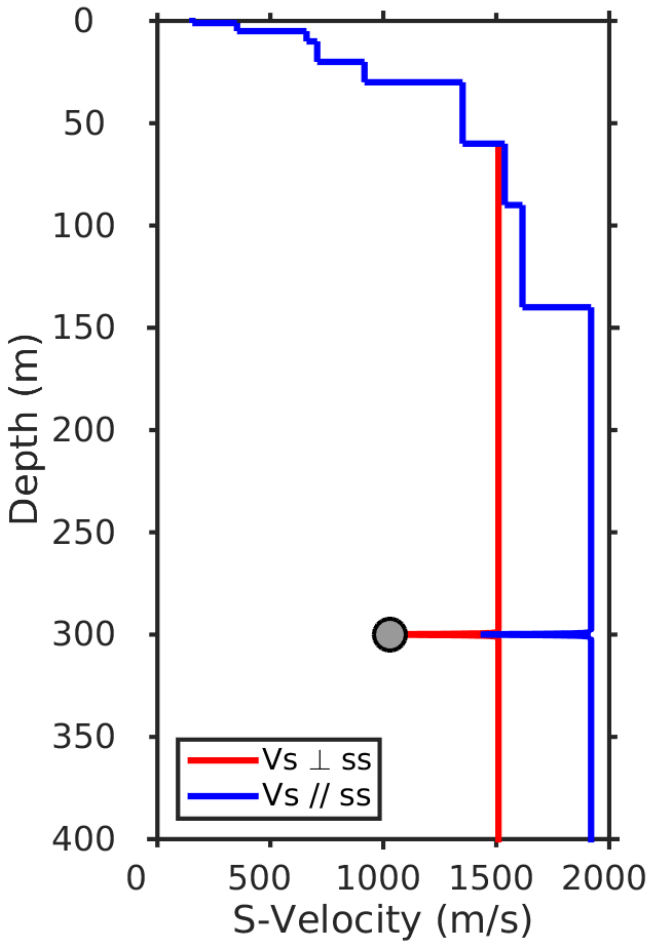

Figure 23 – *Extended velocity profile of Mont Terri, obtained by interpretation merging of the results from the rock laboratory experiment and the ambient vibration survey. The location of the tunnel is schematically indicated with the gray dot.*

Computation of the ground motion at 300m depth was performed analytically, using SH-wave transfer function formalism. With respect to the amplification computed assuming free-surface conditions within the tunnel (**Figure 24**A) the ground motion model obtained when accounting for the full-wave propagation along the extended profile presents the typical troughs due to negative interference of up-going and down-going reflected waves (**Figure 24**B). In comparison, empirical results from spectral modeling (EMS) lay somewhere in between the two predicted models. This is due to different reasons: the effect of tunnel free-surface, the presence of complex phenomena (like scattering) hardly captured by the analytical model and the uncertainty on the velocity profile.

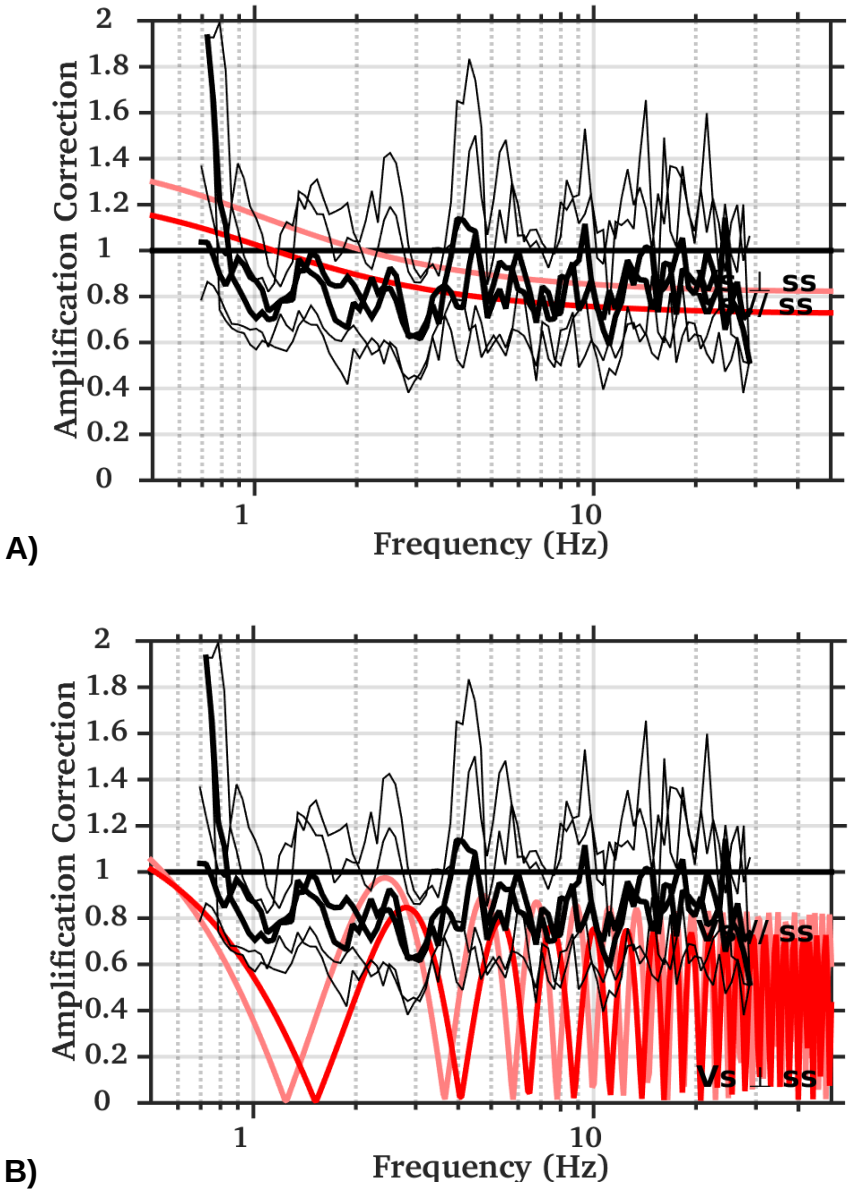

Figure 24 – *Comparison of the SH-wave amplification functions at the stations MTI1 and MTI2 considering A) free-surface approximation at laboratory depth and B) full wave-propagation along the extended velocity profiles.*

REFERENCES

Bonnefoy-Claudet S., Cotton F., and Bard P.-Y.. The nature of noise wavefield and its applications for site effects studies. *Earth-Science Reviews*, 79(3-4): 205–227, December 2006. doi: 10.1016/j.earscirev.2006.07.004.

Burjánek J., Gassner-Stamm G., Poggi V., Moore J. R., and Fäh D.. Ambient vibration analysis of an unstable mountain slope. *Geophysical Journal International*, 180(2):820–828, 2010. doi: 10.1111/j.1365-246X.2009.04451.x.

Capon J.. High-Resolution Frequency-Wavenumber Spectrum Analysis. *Proceedings of the IEEE*, 57(8):1408–1418, 1969.

CEN. *Eurocode 8: Design of structures for earthquake resistance - Part 1: General rules, seismic actions and rules for buildings*. European Committee for Standardization, en 1998- 1: edition, 2004.

Edwards, B., Michel, C., Poggi, V., & Fäh, D. (2013). Determination of Site Amplification from Regional Seismicity: Application to the Swiss National Seismic Networks. *Seismological Research Letters*, *84*(4), 611–621. doi:10.1785/0220120176

Fäh D., Kind F., and Giardini D.. A theoretical investigation of average H/V ratios. *Geophysical Journal International*, 145:535–549, 2001.

Fäh D., Stamm G., and Havenith H.-B.. Analysis of three-component ambient vibration array measurements. *Geophysical Journal International*, 172(1):199–213, 2008. doi: 10.1111/j.1365-246X.2007.03625.x.

Fäh D., Wathelet M., Kristekova M., Havenith H.-B., Endrun B., Stamm G., Poggi V., Burjanek J., and Cornou C.. Using Ellipticity Information for Site Characterisation Using Ellipticity Information for Site Characterisation. Technical report, NERIES JRA4 Task B2, 2009.

Freivogel M., Huggenberger P. Modellierung bilanzierter Profile im Gebiet Mont Terri-La Croix (Kanton Jura). In: Heitzmann P, Tripet JP (eds) Mont Terri Project Geology, Paleohydrology and Stress Field of the Mont Terri Region, Reports of the Federal Office for Water and Geology, 2003.

Konno K. and Ohmachi T.. Ground-Motion Characteristics Estimated from Spectral Ratio between Horizontal and Vertical Components of Microtremor. *Bulletin of the Seismological Society of America*, 88(1):228–241, 1998.

Poggi V. and Fäh D.. Estimating Rayleigh wave particle motion from three-component array analysis of ambient vibrations. *Geophysical Journal International*, 180(1):251–267, 2010. doi: 10.1111/j.1365-246X.2009.04402.x.

Poggi V., Edwards B. and Fäh D.. Derivation of a Reference Shear-Wave Velocity Model from Empirical Site Amplification. *Bulletin of the Seismological Society of America*, *101*(1), 258–274, 2011. doi:10.1785/0120100060

Poggi V., Fäh D., Burjanek J., and Giardini D.. The use of Rayleigh-wave ellipticity for site-specific hazard assessment and microzonation: application to the city of Lucerne, Switzerland. *Geophysical Journal International*, 188(3):1154–1172, 2012. doi: 10.1111/j.1365-246X.2011.05305.x.

Roesset J.M.. Fundamentals of soil amplification. In R. J. Hansen, editor, *Seismic Design for Nuclear Power Plants*, pages 183–244. M.I.T. Press, Cambridge, Mass., 1970.

SIA. *SIA 261 Actions sur les structures porteuses*. Société suisse des ingénieurs et des

architectes, Zürich, SIA 261:20 edition, 2003.

Wathelet M.. An improved neighborhood algorithm: Parameter conditions and dynamic scaling. *Geophysical Research Letters*, 35(9):1–5, 2008. doi: 10.1029/2008GL033256.

APPENDIX – Examples of relevant seismic logs

A) Report GBD23

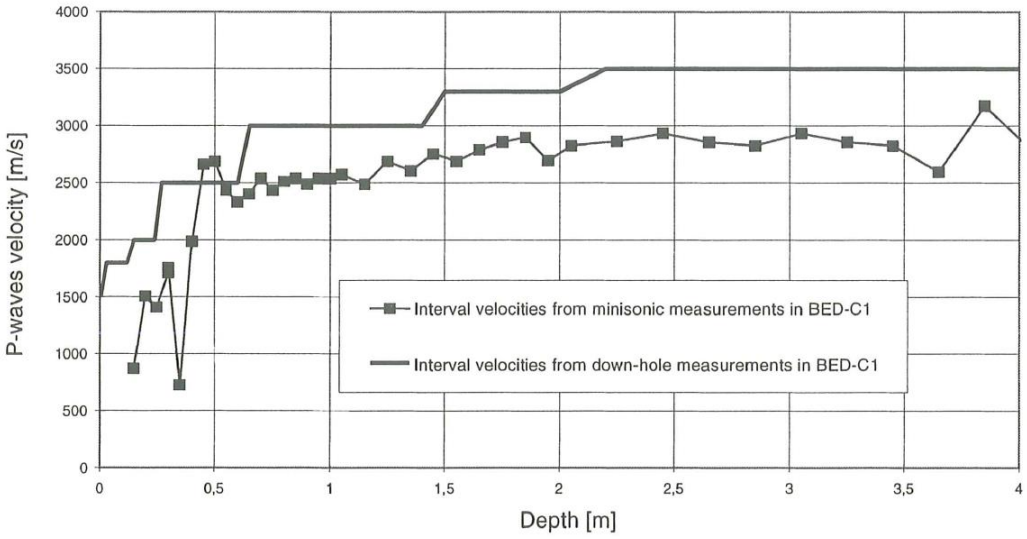

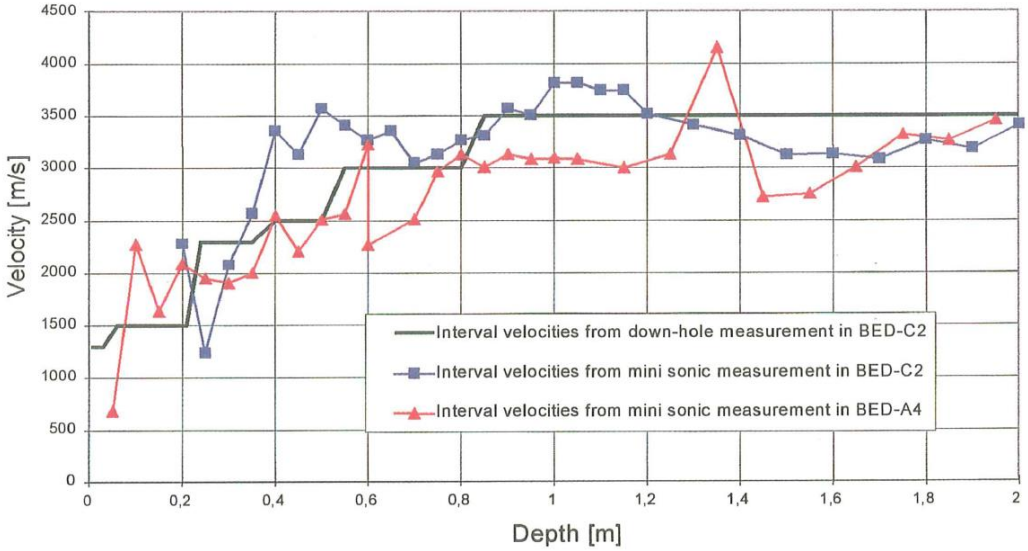

B1) Report TN97-33S

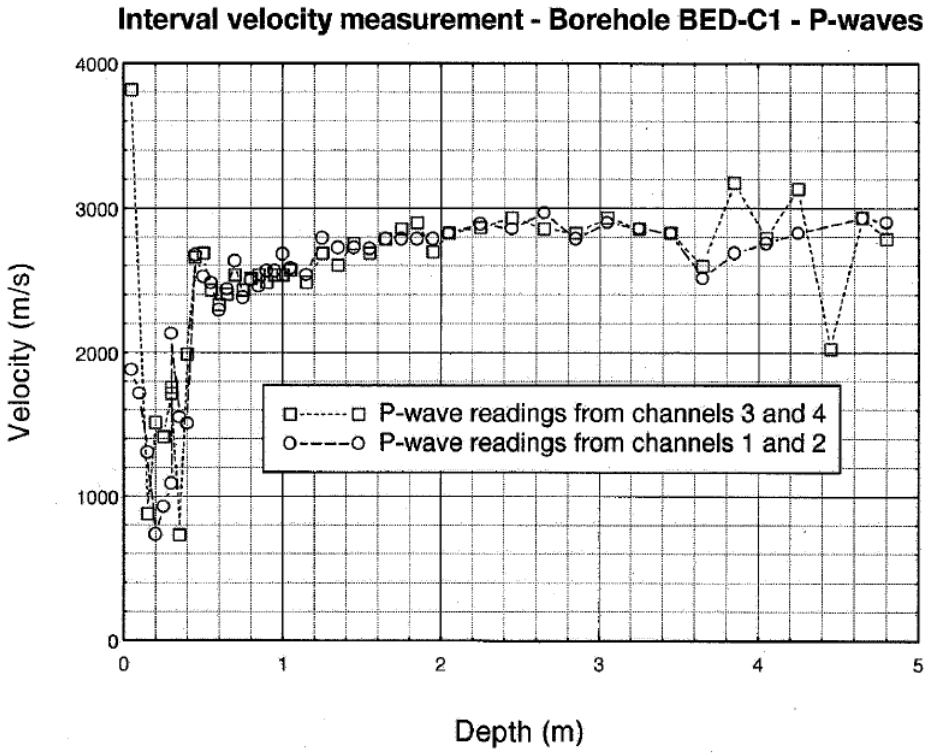

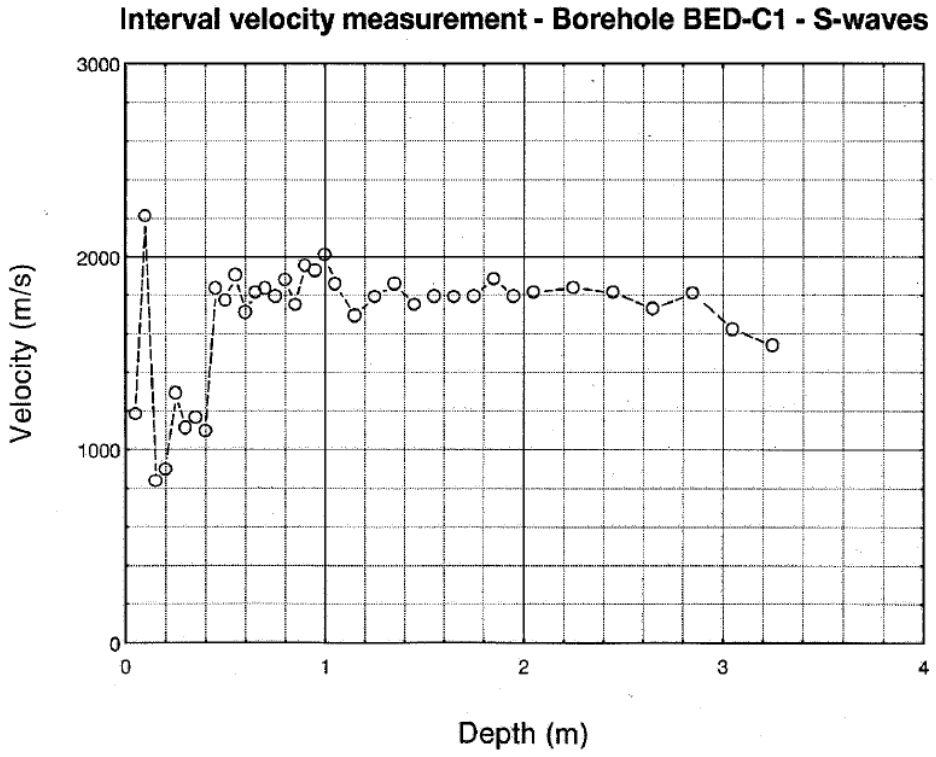

B2) Report TN97-33S

Interval velocity measurement - Borehole BED-A4 - P and S-waves

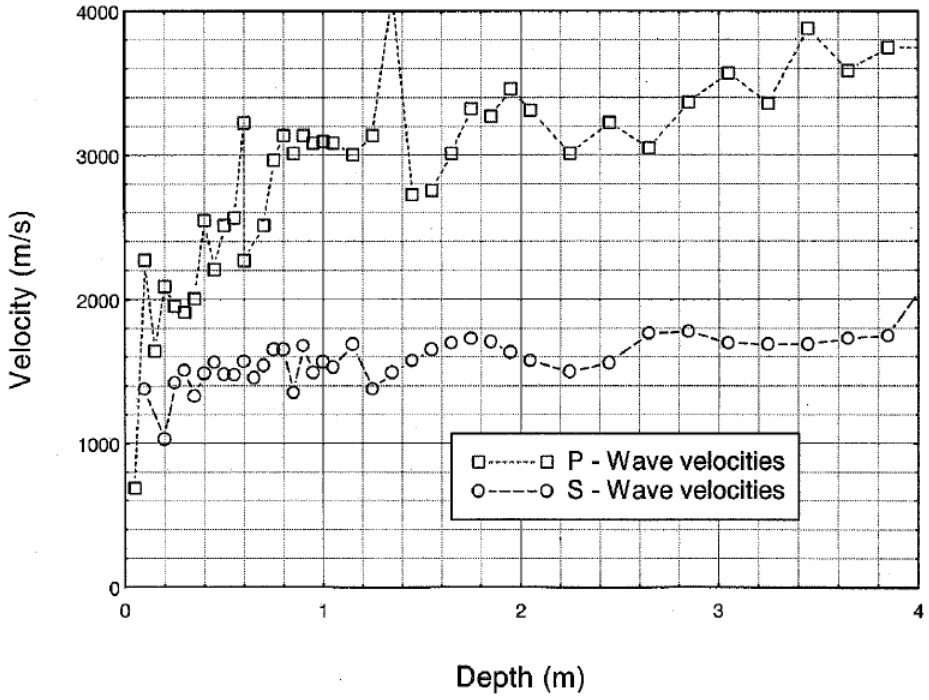

Interval velocity measurement - Borehole BED-C2 - P and S-waves

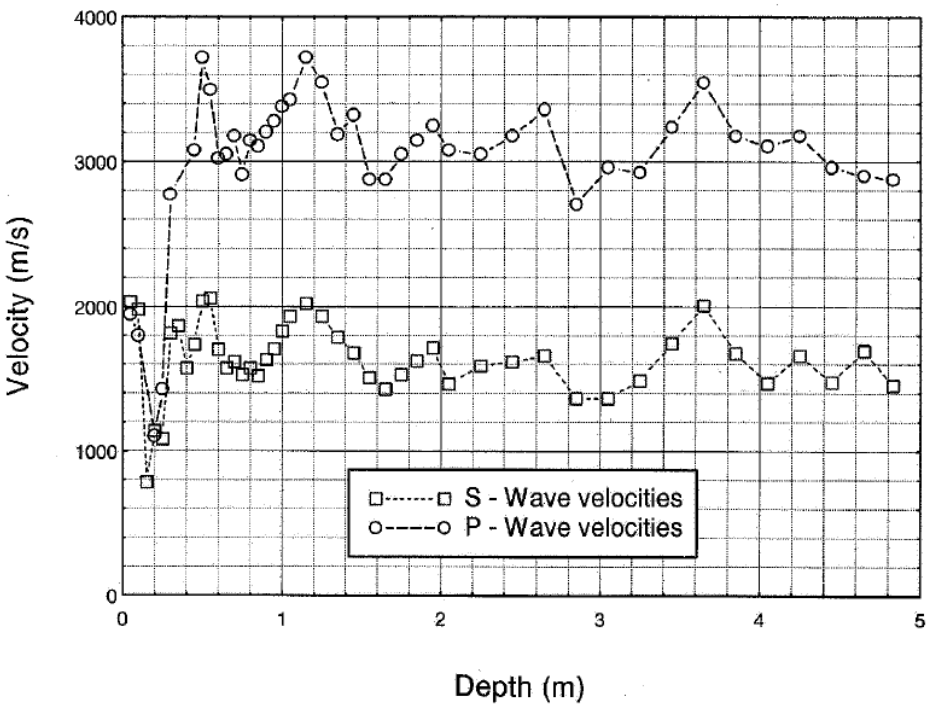

C) Report TN2002-4

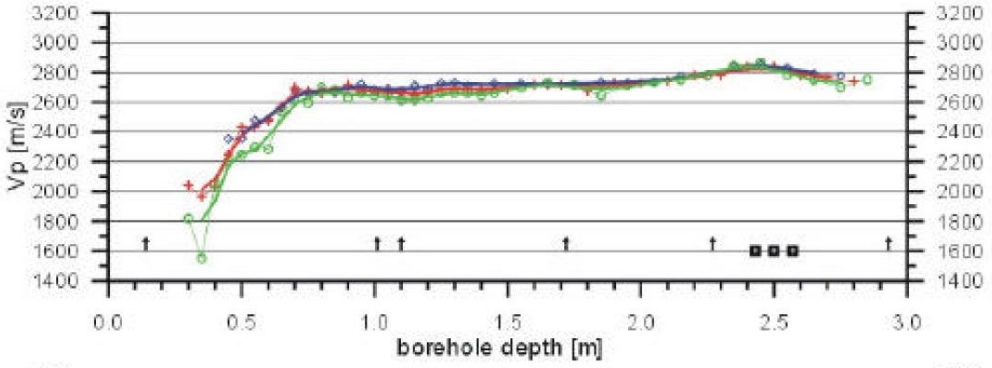

B10

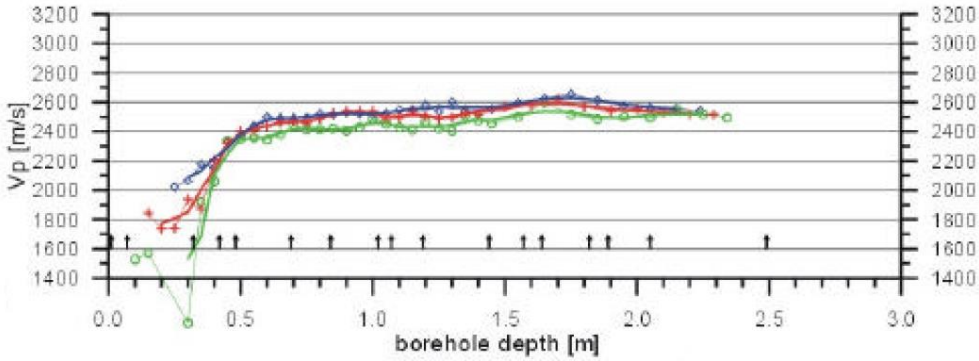

B11

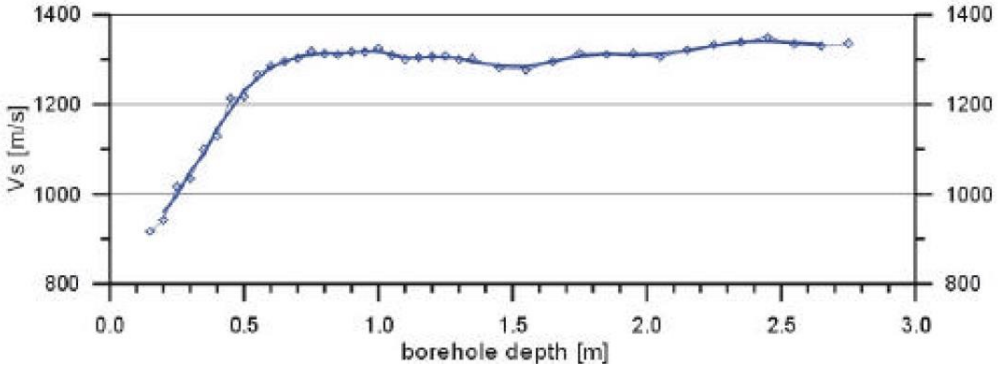

B10

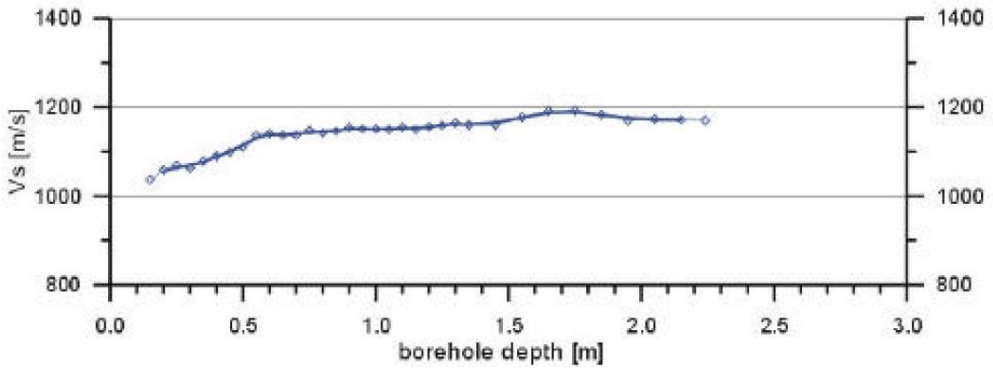

B11